Fluid-structure interaction simulation of tissue degradation and its effects on intra-aneurysm hemodynamics

Haifeng Wang[a]*, Klemens Uhlmann[b], Vijay Vedula[c], Daniel Balzani[b], Fathollah Varnik[a]*

[a]Interdisciplinary Centre for Advanced Materials Simulation (ICAMS), Ruhr-University Bochum, Germany
[b]Continuum Mechanics, Ruhr-University Bochum, Germany
[c]Department of Mechanical Engineering, Columbia University in the City of New York, New York, United States

*Correspondence: haifeng.wang@rub.de (HW); fathollah.varnik@rub.de (FV)

Abstract

Tissue degradation plays a crucial role in vascular diseases such as atherosclerosis and aneurysms. We present a novel finite element method-based approach to model the microscopic degradation of an aneurysmal wall due to its interaction with blood flow. The model is applied to study the combined effects of pulsatile flow and tissue degradation on the deformation and intra-aneurysm hemodynamics. Our computational analysis reveals that tissue degradation leads to a weakening of the aneurysmal wall, which manifests itself in a larger deformation and a smaller von Mises stress. Moreover, simulation results for different heart rates, blood pressures and aneurysm geometries indicate consistently that, upon tissue degradation, wall shear stress increases near the flow-impingement region and decreases away from it. These findings are discussed in the context of recent reports regarding the role of both high and low wall shear stress for the progression and rupture of aneurysms.

1 Introduction

Microscopic degradation in vascular tissue is a severe pathological process and is associated with cardiovascular diseases such as aneurysms with high mortality [1, 2, 3].

Hemodynamic forces, such as pressure and wall shear stress (WSS, defined as the tangential stress component induced by the flowing blood on the vascular walls), play a crucial role in cardiovascular physiology and pathology by affecting the biochemical response of the surrounding tissue [4, 5, 6]. Arterial wall tissue gradually changes under abnormal WSS and other biological factors (long-term effect). The resulting change of arterial geometry, on the other hand, alters the flow characteristics (short-term effect). Both low WSS [7, 8, 9] and high WSS [10, 11, 12] have been associated with the progression and rupture

of aneurysms. To reconcile these conflicting observations, Meng et al. [13] have proposed two independent pathways for the mechanistic link between hemodynamic forces and aneurysm's pathological changes. Low WSS is related to the inflammatory cell-mediated destructive remodeling of the arterial wall; high WSS, which is prevalent near the flow impingement site, is associated with the mural cell-mediated remodeling. High blood pressure is also known to be responsible for further degradation and enlargement of the aneurysm.

Despite their significance, however, it is difficult to clinically measure the spatial distribution and temporal evolution of WSS and pressure inside the aneurysm dome. Numerical simulations provide a promising alternative. The previous study has shown that blood flow inside an aneurysm exhibits complex features (such as flow disturbances) associated with wall softness [14]. Also fluid-structure interaction (FSI) simulations with complex wall models [15] have shown significant effects on WSS even in simplified arteries. To date, however, we are not aware of any numerical study that couples hemodynamics with the progression of tissue degradation and vessel wall softening.

We propose a novel FSI model capable of accounting for the interaction of blood flow with arterial walls and simultaneously capturing the degradation of vascular tissue. The coupled model is first benchmarked on a canonical problem and is then used to study the effect of tissue degradation on the spatial distribution of strain, WSS and pressure in aneurysms. Upon degradation, we observe a weakening of the vessel wall resulting in larger strain and smaller stress magnitude. Remarkably, WSS increases (up to 20%) near the flow-impingement region but decreases away from it. Near-wall pressure, however, changes only slightly upon tissue degradation.

2 Methods

We have developed a new computational framework by combining a tissue degradation model [16, 17] and a finite element-based FSI solver [18]. A brief description of the individual components is given below.

2.1 Tissue degradation model

The damage accumulation is modeled across two phenomenological fiber families. The strain energy functions of the tissue degradation model are shown in Appendix A.

The scalar damage functions, D_i, for each fiber family $i = 1, 2$, used to capture remnant strains (i.e., strain at zero stress level after unloading) within the fibers and the *stress-softening* effect, is defined as

$$D_i(\beta_i) = D_{\mathrm{s},\,i}\left[1 - \exp\left(\frac{\ln(1 - r_{\mathrm{s}})}{\beta_{\mathrm{s}}}\beta_i\right)\right], \tag{1}$$

where the maximally reachable damage value for fixated load levels is denoted by $D_{\mathrm{s},\,i} \in [0, 1)$, the fraction of the maximum damage is $r_{\mathrm{s}} = 0.99$, and $\beta_{\mathrm{s}} > 0$

is the value of the internal variable β_i corresponding to damage saturation. The internal variable is defined as $\beta_i = \langle \tilde{\beta}_i - \tilde{\beta}_i^{\mathrm{ini}} \rangle$, with $\tilde{\beta}_i = \int_0^t \langle \dot{\Psi}_i^{\mathrm{ti},\,0}(s) \rangle \mathrm{d}s$ allowing for continuous damage evolution for loading and re-loading paths and $\tilde{\beta}_i^{\mathrm{ini}}$ denoting the damage initiation threshold. The latter is set equal to $\tilde{\beta}_i$ in the scenario where the transition from physiological to supra-physiological loading is reached. Thereby, it is a locally distributed quantity depending on the boundary value problem under investigation and not a material parameter. t indicates the time at the current state, and $\dot{\Psi}_i^{\mathrm{ti},\,0}$ is the first time derivative of the fictitiously undamaged (effective) strain energy density $\Psi_i^{\mathrm{ti},0}$ in fiber direction i. The maximally reachable damage value for fixated load levels $D_{\mathrm{s},\,i}$ is expressed as

$$D_{\mathrm{s},\,i}(\gamma) = D_\infty \left[1 - \exp\left(\frac{\ln(1 - r_\infty)}{\gamma_\infty} \gamma_i \right) \right], \tag{2}$$

with the predefined converging limit for the overall damage value $D_\infty \in [0, 1)$ and $\gamma_\infty > 0$ representing the value of the internal variable γ_i reached at the limit fraction $r_\infty = 0.99$.

In order to ensure that $D_{\mathrm{s},\,i}$ remains unchanged during a cyclic process under fixed maximum load levels, the second internal variable

$$\gamma_i = \max \langle \Psi_i^{\mathrm{ti},\,0}(s) - \Psi_{\mathrm{ini},\,i}^{\mathrm{ti},\,0} \rangle, \;\; s \in [0, t] \tag{3}$$

is defined as the maximum value of the effective energy reached up to the current state at t. $\Psi_{\mathrm{ini},\,i}^{\mathrm{ti},\,0}$ denotes the effective strain energy density at an initial damage state obtained at the limit of the physiological domain. The damage saturation criterion is expressed as

$$\phi_i := \langle \Psi_i^{\mathrm{ti},\,0}(s) - \Psi_{\mathrm{ini},\,i}^{\mathrm{ti},\,0} \rangle - \gamma_i \leq 0. \tag{4}$$

Note that various alternative approaches for the description of tissue degradation have been proposed in the literature, see e.g. [19, 20, 21, 22]. The degradation model considered here has been validated in previous studies [16, 17] and shown to correspond well with cyclic experiments performed on different types of arteries. An application of the model to aneurysm is, however, new. In this context, it is noteworthy that pathological tissue remodeling often plays a key role in cerebral aneurysm. The model used in the present study does not account for this effect. However, the focus of the present investigation is not on long-time degradation processes, where tissue remodeling is of key importance, but on the combined effect of flow-induced forces and short-time degradation which occurs during a few cardiac cycles. Thus, this study has a qualitative character and presents a first step in a long-time effort towards a more realistic model.

In numerical simulations, a loss of ellipticity may be observed when including material stiffness degradation rendering the mesh-dependent. In this case, either a relaxed damage formulation [23] or a gradient-enhanced approach [24] may be applied. In the present paper, however, numerical analysis have shown mesh-convergence and thus, such more advanced formulations were not considered.

2.2 FSI solver

We approximate blood as an incompressible Newtonian fluid. For fluid-structure interactions, we employ the well-developed, validated and open-sourced finite element method-based solver, SimVascular/svFSI [18], which uses an arbitrary Lagrangian-Eulerian formulation of Navier-Stokes equations to model incompressible flows on moving domains [25]. It has been applied to a variety of applications including blood flow in developing ventricles [5], patient-specific studies including pulmonary hypertension and coronary artery bypass graft [26], and FSI simulations in aortic dissections [27]. Since the methodology involved in the FSI solver is rather standard, it is not repeated here. For further details, the reader is referred to [25, 27].

For the flow boundary conditions, we prescribe a pulsatile flow at the inlet with a parabolic velocity profile (Fig. 1). We prescribe a three-element Windkessel-type boundary condition at each outlet and the parameters are tuned to match the systolic, diastolic and mean blood pressures (subsection 2.4). At each cross-sectional end of the structural domain, we apply homogeneous Dirichlet boundary conditions to anchor its location.

2.3 Verification of the coupling between the damage model and the FSI-solver

The coupling between our in-house tissue damage subroutine and the FSI is facilitated via the exchange of the strain and stress fields. The deformation gradient tensor, $\boldsymbol{F}$ of the vessel wall computed at the integration point-level and other user-provided parameters are passed as input to our in-house material subroutine. The subroutine then returns the second Piola Kirchhoff stress tensor and the corresponding elasticity tensors to the FSI solver. The FSI-solver Simvascular/svFSI, in turn, solves for the displacement field of the vessel wall and the blood velocities and pressure, using a monolithic coupling between the structural dynamics and the Navier-Stokes equations.

To validate the coupling between the FSI solver and the tissue-degradation material routine, we use a canonical problem where a cube is subjected to a uniaxial tension (see Fig. 2(a)). The Cauchy stress versus strain profiles, without and with damage model, obtained using the proposed numerical framework are compared against those obtained from FEAP software package [16]. However, as FEAP is primarily a solid mechanics software, we do not model the blood flow for this verification exercise. Instead, we use svFSI as a pure solid mechanics solver that interfaces with our in-house material subroutine. All relevant simulation parameters are given in Table 1.

We show a very strong agreement in Cauchy stress versus strain profiles between the present numerical framework and FEAP (Fig. 2(a)).

The material parameters used in this study are listed in Table 1. As illustrated in Fig. 2(b), other choices of degradation intensity and the rate of damage saturation can be also simulated by adapting the damage parameters γ_∞ and β_s, respectively. Indeed, the material parameters given in Table 1 can be eas-

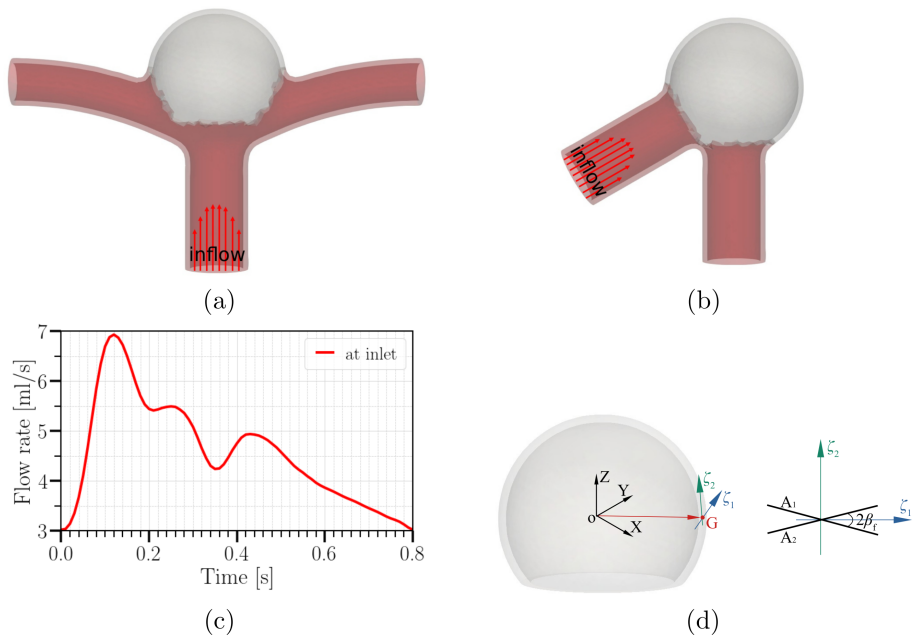

Fig 1: (a–b) Geometries studied in this work; (a) an idealized internal carotid artery bifurcation aneurysm (based on the data in [28, 29]); (b) idealized aneurysm based on the data in [30]. The spherical caps (aneurysms) in (a) and (b) have identical sizes; the diameter of the two vessels in (b) is the same as that of the parent vessel in (a). Arrows highlight the parabolic velocity profile imposed at the inlet. The tissue degradation model is applied only on the aneurysmal region (colored in grey); the remaining of the vessel (red) is modeled as Neo-Hookean. (c) Temporal variation of the imposed flow rate at the inlet [31]. (d) Fiber orientations in a spherical aneurysm (as adopted by [32]). Two fiber families, $\boldsymbol{A}_1$, $\boldsymbol{A}_2$, are applied at each Gauss integration point G, where $\boldsymbol{A}_i = \cos(\beta_{\mathrm{f}}^i)\boldsymbol{\zeta}_1 + \sin(\beta_{\mathrm{f}}^i)\boldsymbol{\zeta}_2$ with $i = 1,\ 2$ and $\beta_{\mathrm{f}}^1 = \beta_{\mathrm{f}}^2$. $\boldsymbol{\zeta}_2 := \boldsymbol{V}_{\mathrm{OG}} \times \boldsymbol{\zeta}_1$; $\boldsymbol{\zeta}_1 := \boldsymbol{V}_{\mathrm{OZ}} \times \boldsymbol{V}_{\mathrm{OG}}$; $\boldsymbol{\zeta}_1 = (1, 1, 0)/\sqrt{2}$ is used in the case that $\boldsymbol{V}_{\mathrm{OG}}$ is parallel to $\boldsymbol{V}_{\mathrm{OZ}}$.

Table 1: Material parameters for a human carotid artery [16]. For the parent and branch vessels outside the aneurysm (Fig. 1(a-b)), elastic modulus and Poisson's ratio are chosen as 1000 kPa [33] and 0.49, respectively. See Appendix A for more details on how the material parameters enter the model.

c_1 [kPa]	ϵ_1 [kPa]	ϵ_2 [-]	α_1 [kPa]	α_2 [-]
9.02	499.8	2.4	1400	2.2
κ [-]	β_{f} [°]	D_∞ [kPa]	γ_∞ [kPa]	β_{s} [-]
1e-8	39.87	0.96	17.98	0.06

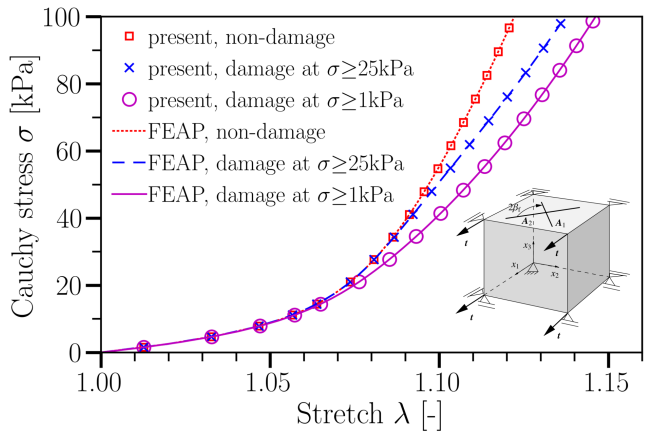

(a)

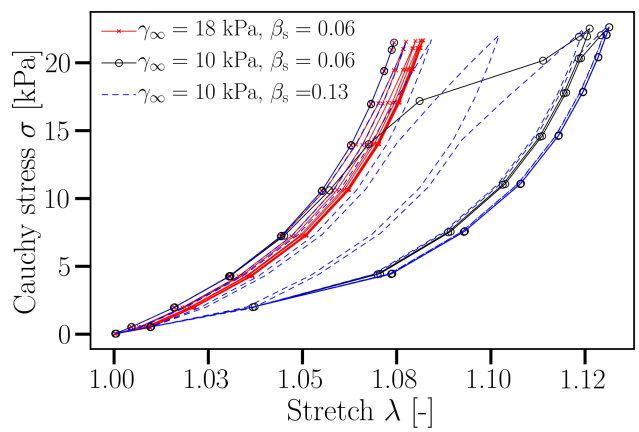

(b)

Fig 2: (a) Uniaxial tension tests using a sample with cubic shape without and with damage. Results are shown for the present hybrid model and FEAP. In all cases, the input load (or transmural pressure) is increased from 0 to 100 kPa linearly with time. As can be seen, simulation results using the hybrid FSI framework and FEAP are identical verifying our implementation. All relevant material parameters are given in Table 1 as all cases considered here are quasi-static. Fiber directions are indicated in the inset; the angle between the two fibers, $\boldsymbol{A}_i$, is $2\beta_{\mathrm{f}}$ with $\beta_{\mathrm{f}} = 39.87$. (b) Cyclic uniaxial tension tests using the same geometry and material parameters as in (a) but different values of γ_∞ and β_s. Each simulation is performed for ten cycles. In all three cases shown, a *cyclic* load is imposed, which varies between 0 and 20 kPa. Degradation process is turned on after the first cycle. As can be seen, the damage parameters, γ_∞ and β_s, control the degradation intensity and rate, respectively.

ily tuned for long-term tissue degradation, provided that reliable experimental and/or clinical data become available.

2.4 Parameters for FSI simulation including material damage

To gain a qualitative understanding of the effects arising from tissue degradation, we perform two sets of simulations: One with degradation switched on and the other switching it off (i.e., assuming a non-degrading tissue), using a bifurcation aneurysm model (Fig. 1(a)).

The inner diameters of the parent vessel and its two branches are 0.41 cm and 0.29 cm [29], respectively. We assume identical branch vessel dimensions to simplify the tuning of the Windkessel parameters (i.e., distal resistance R_d, proximal resistance R_p and capacitance C (RCR)) at each outflow branch. The inner diameter of the spherical cap (aneurysm) is 1.0 cm in this work. Wall thickness is 0.04 cm and spatially homogeneous.

The time dependence of the flow rate at the inlet is based on the data from [31] (Fig. 1(c)). The mean inlet flow rate is $Q_\mathrm{in} = 4.6$ ml/s (range: 3.0–6.9 ml/s). The duration of cardiac cycle is 0.8 seconds. The flow rate at each branch is $Q_\mathrm{b} = 0.5 Q_\mathrm{in}$.

Pulse pressure, i.e., the difference between systolic and diastolic blood pressures, in most people is between 40 and 60 mmHg. A small increase (e.g., by 10 mmHg) in the pulse pressure often significantly increases the cardiovascular risk (e.g., by 20%) [34]. In this study, the peak systolic and end diastolic blood pressures are 140 mmHg and 70 mmHg (mean: 100 mmHg), respectively, similar to the hypertension cases reported in [35]. The total resistance at each branch is $R_\mathrm{tot,b} = 5.7{\cdot}10^4$ g cm^{-4} s^{-1} to meet the pressure shown. The distal and proximal resistance at each outlet is given by $R_\mathrm{d,b} = k_\mathrm{d} R_\mathrm{tot,b}$, and $R_\mathrm{p,b} = (1 - k_\mathrm{d}) R_\mathrm{tot,b}$, where the factor k_d defines the ratio of distal to total resistance and is fixed for all outlets to $k_\mathrm{d} = 0.9$ [36]. The capacitance at each branch is identical and equal to 10^{-6} cm^4 s^2 g^{-1}. Fluid density and viscosity are $\rho_\mathrm{f} = 1.055$ g cm^{-3} and $\eta_\mathrm{f} = 0.04$ g cm^{-1} s^{-1}, respectively. In all FSI simulations, the solid density is $\rho_\mathrm{s} = 1.2$ g cm^{-3}. The discretized time step is 10^{-4} s.

The fiber orientations applied for the aneurysm dome are indicated in Fig. 1(d). Due to the lack of experimental and clinical data on the fiber orientations of any aneurysms, we set $\beta_\mathrm{f} = 40°$ as in [16]. The other parameters of the material model are listed in Table 1.

2.5 Metrics for analysis

Hemodynamic quantities play an important part in mechanobiological development of vascular diseases [37]. Among these, WSS and time-averaged wall shear stress (TAWSS) are often reported to be closely associated with the formation and rupture of aneurysms [13, 38].

The TAWSS at an arbitrary position $\boldsymbol{x}$ is simply the average magnitude of the WSS vector $\boldsymbol{\tau}_{\mathrm{w}}$ over one cardiac cycle of duration T

$$\mathrm{TAWSS}(\boldsymbol{x}) = \frac{1}{T}\int_0^T |\boldsymbol{\tau}_{\mathrm{w}}(\boldsymbol{x}, t)| \ \mathrm{d}t. \tag{5}$$

To quantify the role of tissue degradation in aneurysmal wall and intra-aneurysm hemodynamics, we also examine the near-wall pressure, von Mises stress and strain magnitude on the aneurysmal wall. We compute the time average of each metric, defined along similar lines as Eq. 5. We further analyze the relative changes in these metrics due to tissue degradation. Given a time-averaged quantity $f(\boldsymbol{x})$ at point $\boldsymbol{x}$, the *relative percentage change* in $f(\boldsymbol{x})$ between the degraded (f^{d}) and non-degraded (f^{nd}) cases is defined via

$$\Delta f(\boldsymbol{x}) = \frac{f^{\mathrm{d}}(\boldsymbol{x}) - f^{\mathrm{nd}}(\boldsymbol{x})}{f^{\mathrm{nd}}(\boldsymbol{x})} \times 100. \tag{6}$$

3 Results and discussion

In this section, we use the proposed numerical model to investigate the effect of tissue degradation on the hemodynamics and the mechanical response of a bifurcation aneurysm model (Fig. 1(a)). We focus on a simplified aneurysm model to assess the feasibility of performing a FSI simulation combined with a material model and develop preliminary insights into the role of hemodynamics on tissue degradation and vice versa. However, extending our numerical framework to performing patient-specific FSI simulations of tissue degradation is straightforward, provided that personalized data on tissue fiber architecture and damage model parameters become available [39, 40].

The development of aneurysm usually takes months or even years [41]. This slow process depends on several physiological and hemodynamic parameters, and is far from being completely understood. However, there is strong clinical evidence supporting the hypothesis that local WSS and blood pressure play a critical role in aneurysm development and rupture [13]. At the same time, the lack of sufficient experimental and clinical data has limited the development of models that adequately account for the long-term dynamics of tissue degradation. Moreover, the computational cost of FSI simulations prohibits us from simulating long-term hemodynamic response to tissue damage, and vice versa. Therefore, we focus on understanding the hemodynamic implications of tissue degradation within a few cardiac cycles.

We ignore the initial transients and focus on the dynamics after five cardiac cycles.

3.1 Effects of tissue degradation

Figure 3 shows the spatial distribution of WSS and hydrostatic pressure at two instants (peak systole and end diastole) both in the presence and absence of

tissue degradation. A close scrutiny of these images provides some first hints towards the effect of tissue degradation but it seems at this stage a bit too early to draw any specific conclusion based on these images.

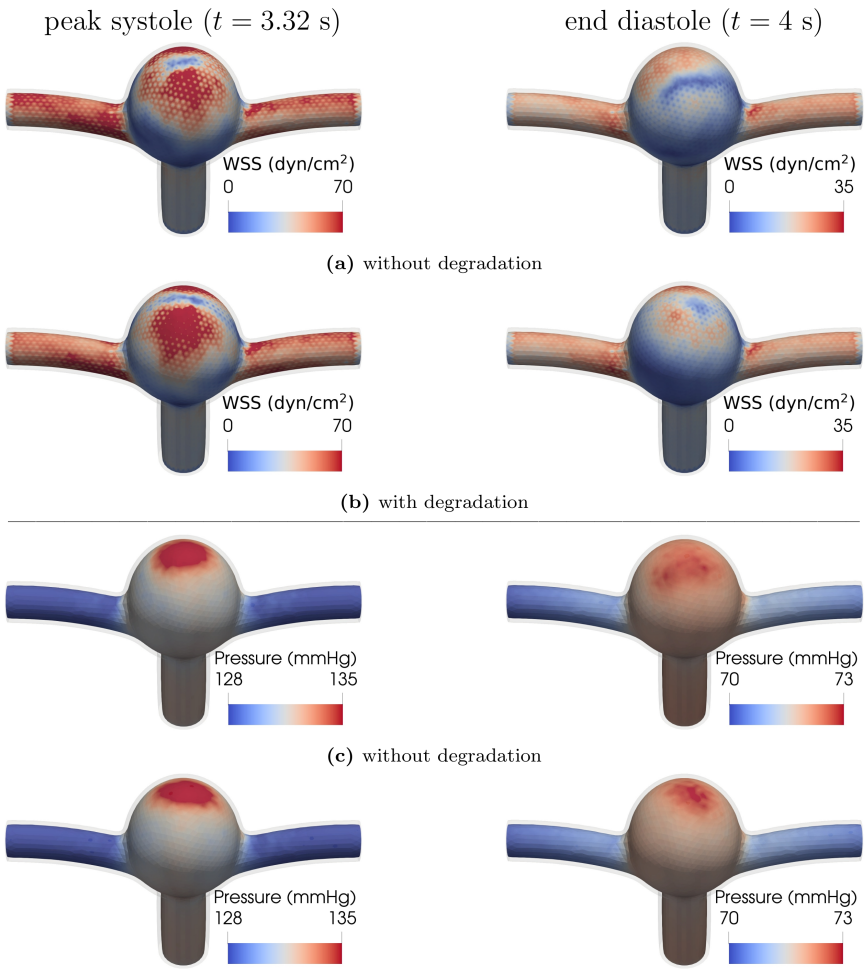

Fig 3: The first two panels show the magnitude of WSS field at (left) peak systole and (right) end diastole (a) without and (b) with tissue degradation. The third and fourth panels present the near-wall pressure field at peak systole and end diastole (c) without and (d) with tissue degradation. Note that the color scales stand for different data ranges in the cases of peak systole and end diastole. The duration of cardiac cycle is $T = 0.8$ s. 1 dyn/cm^2 = 0.1 Pa.

To highlight effects of tissue degradation in a more telling way, we use Eq. 6 and determine the *percentage changes* due to degradation in the above men-

tioned quantities of interest. Using this approach, the increase or decrease of a quantity upon tissue-degradation shows itself in a positive or negative value, and will be made visible by red or blue color, respectively.

As illustrated in Fig. 4, this analysis reveals that tissue degeneration leads to a reduction of von Mises stress and an increase in strain at the same time. This is direct evidence for a substantial decrease of tissue-stiffness due to degradation in the present material model. Thus, the current approach is able to account for *stress softening*, a phenomenon commonly observed in biological tissues.

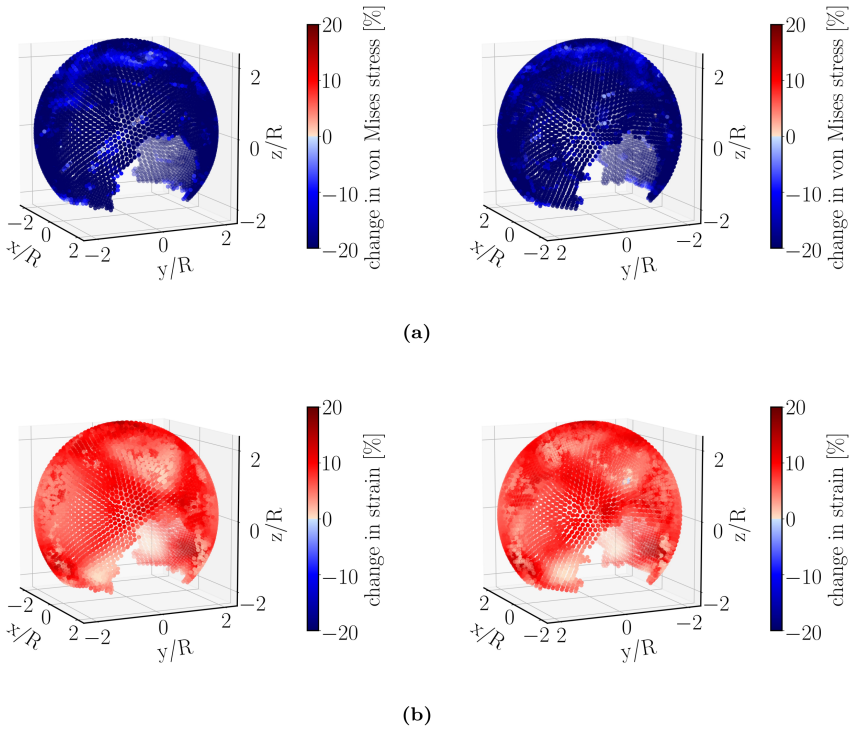

Fig 4: Relative percentage change (Eq. 6) of (a) von Mises stress and (b) strain magnitude of the aneurysmal wall between non-degraded and degraded cases. All quantities are first averaged over a full cardiac cycle (similar to Eq. 5) and then inserted into Eq. 6 to obtain the relative change due to degradation. It is seen from these plots that including degradation leads to an increase in strain and a decrease in von Mises stress. The right panels show the same simulated data as in the left ones but after rotating the aneurysm dome by an angle of π around the polar axis.

Moreover, degradation effects seem to be quite heterogeneous. This heterogeneity is strongly enhanced in the case of TAWSS (Fig. 5(a)).

In contrast to its rather strong effects on WSS, tissue degradation has a marginal influence on the near-wall pressure. To highlight this issue, we have

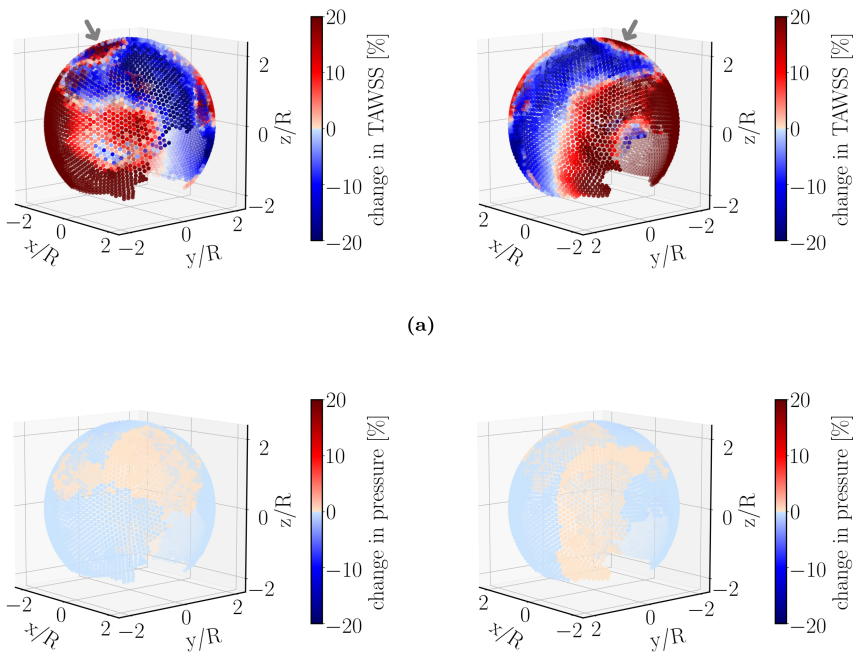

(a)

(b)

Fig 5: Relative percentage change (Eq. 6) of (a) TAWSS and (b) near wall pressure. TAWSS shows a significant effect of degradation (roughly 20% variation) and is spatially heterogeneous. Moreover, tissue degradation leads to an increase of TAWSS near the flow-impingement region as indicated by the arrow. Near-wall pressure, however, is rather insensitive to degradation. The right panels show the same simulated data as in the left ones but after rotating the aneurysm dome by an angle of π around the polar axis.

used the same color scale both for pressure and TAWSS. The small variation in pressure upon degradation thus translates into a pale color in Fig. 5(b). The fluid velocity field inside the bifurcation aneurysm is shown in Fig. 6. With the flow entering the aneurysmal sac, complex flow develops, which impinges on the aneurysmal apex and recirculates inside the dome and leads to the formation of eddies.

The impingement of the flow leads to an increase in the local pressure and WSS around the apex of the aneurysm (Fig. 3). This sharp increase in pressure and WSS is of potential clinical interest as it may cause further degradation or even injury to endothelial cells, and thus affect the progression of the aneurysm. Our results indicate that the complexity of the vortical structures is further amplified with tissue degradation (in particular, during diastole as indicated in Fig. 6). We believe that these unsteady variations are primarily responsible for

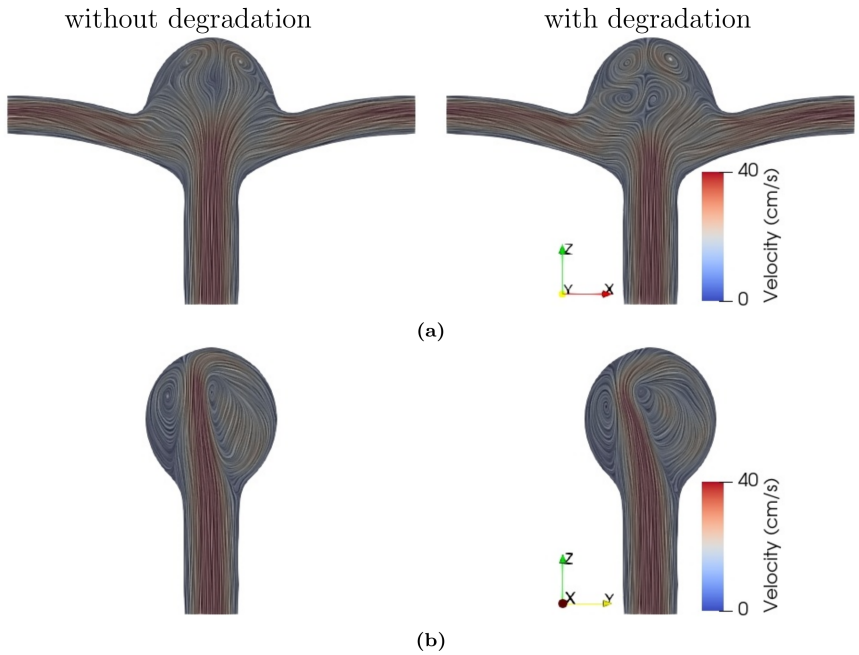

Fig 6: Flow velocity field in the (a) midplane and (b) midway between the two outlets of the bifurcation aneurysm at time instant $t = 4$ s (end diastole), (left) without and (right) with degradation. The duration of cardiac cycle is $T = 0.8$ s. The color scale gives the magnitude of flow velocity. Streamlines serve to visualize the flow pattern.

the heterogeneity in WSS.

Furthermore, Fig. 5(a) suggests that tissue-degradation leads to locally large WSS at areas close to the flow impingement site within the aneurysm dome. Irrespective of the details, this feature seems to be robust and persists under different flow conditions, e.g., by varying the blood pressure and/or heart-beat (see Fig. 7).

This is an important observation since both high WSS prevalent in the flow-impingement region and low WSS at regions away from it have been associated with the degradation and rupture of aneurysmal walls [7, 8, 9, 10, 11, 12, 42]. To examine the connection between WSS and flow impingement further, we have performed a new set of simulations using a different geometry as shown in Fig. 1(b). Again, an increase (decrease) in local WSS is observed at areas close to (far from) the flow impingement zone (Fig. 8(b)).

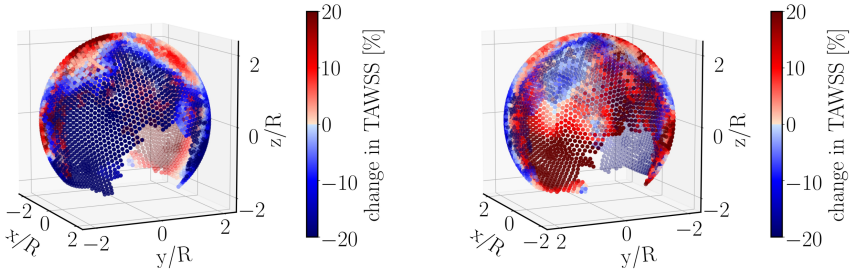

(a) $T = 0.8$ s; pressure = 160/90 mmHg

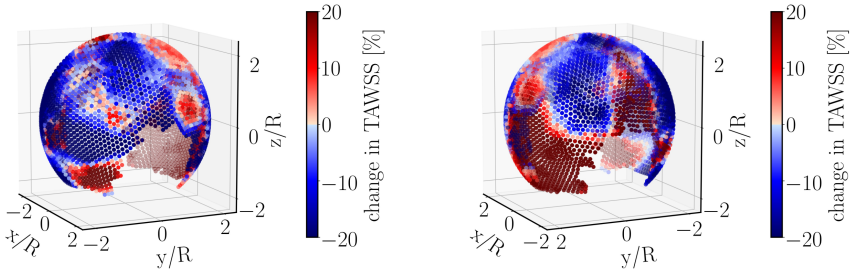

(b) $T = 0.6$ s; pressure = 160/90 mmHg

Fig 7: Relative percentage change of TAWSS under different flow conditions. Compared to the data shown in Fig. 5(a), only the range of blood pressure is changed in (a). Panels in (b) differ from (a) in the duration T of a single heartbeat. The right panels show the same simulated data as in the left ones but after rotating the aneurysm dome by an angle of π around the polar axis.

4 Conclusion

In this study, we presented a hybrid model which combines a solver for dynamics of blood flow and fluid-structure interactions with a material model for tissue degradation. The coupling scheme was successfully tested and then applied to study how flow under the impact of tissue degradation may influence the mechanical state (which, in turn, may affect fluid flow due to changes in arterial wall geometry and deformability) in a bifurcation aneurysm. The time scale of the process considered in this work was purposely restricted to a few cardiac cycles as reliable data on the long-time evolution of tissue damage are currently missing.

The results obtained within this work revealed a strong heterogeneity in the effects arising from degradation on WSS. Importantly, upon degradation, we found increased WSS at places close to the flow-impingement site and decreased WSS beyond the impingement region. This observation is found to be robust

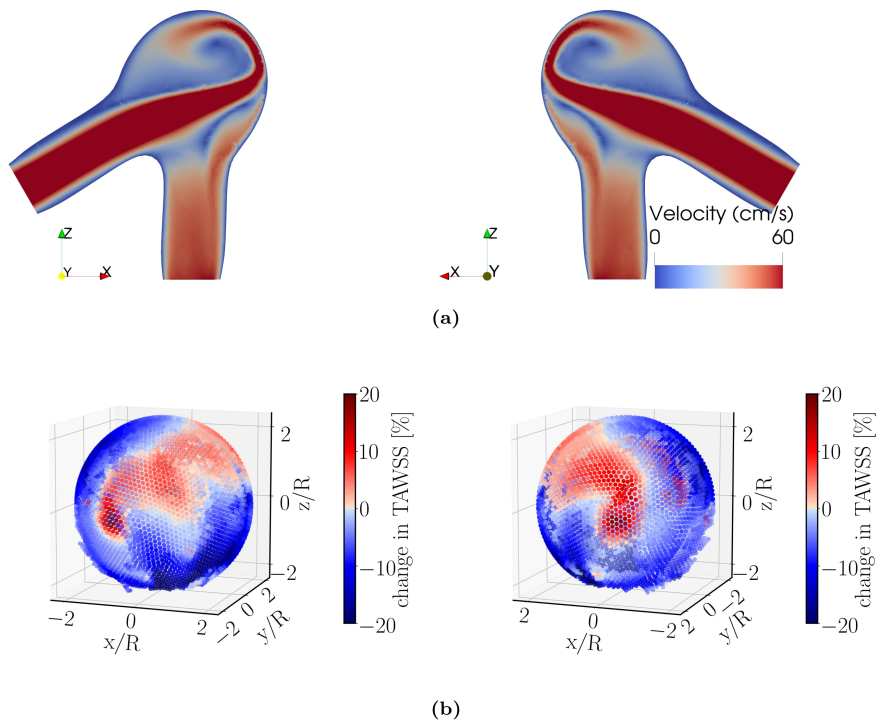

Fig 8: (a) Flow velocity field at peak systole in the presence of degradation. (b) Relative percentage change of TAWSS in the aneurysm dome of the geometry shown in (a). The blood pressure ranges from 90 to 160 mmHg. $T = 0.6$ s. The right panels show the same simulated data as in the left ones but after rotating the aneurysm dome by an angle of π around the polar axis.

and is underlined by simulations of different blood pressures and heart rates. We also present simulated data for a different geometry, confirming this behavior. The set of data provided in this manuscript is thus manifold and supports the proposed connection between effects of degradation and flow impingement on WSS consistently.

Hence, flow impingement seems to be a relevant aspect for a local increase in WSS due to tissue degradation under variable hemodynamic conditions. It would be very interesting to explore possible physiological consequences of this finding for aneurysm's pathological changes.

The present material model can be directly improved if the parameters given in Table 1 are accurately determined via experimental and clinical tests. Many simplifications are made in this work. It thus remains a task for future work to account for, e.g., patient-specific aneurysm model, non-Newtonian blood flow, tissue growth and remodeling processes, and realistic fiber orientations. Moreover, it would be a phenomenal progress to go beyond a few cardiac cycles and

develop a reliable model for long-term tissue degradation (in particular, fatigue under cyclic loading).

Appendix A Strain energy functions

The total strain energy function of the tissue degradation model is chosen to be

$$\Psi^{\text{tot}} = \Psi^{\text{iso}} + \Psi^{\text{vol}} + \sum_{i=1}^{2} \Psi_i^{\text{ti}}. \tag{7}$$

The first term on the rhs of Eq. (7) is the isotropic part describing the ground matrix material, which is modeled by the incompressible Neo-Hookean model $\Psi^{\text{iso}} = c_1(I_1/I_3^{1/3} - 3)$. The second term is the compressible function $\Psi^{\text{vol}} = \epsilon_1(I_3^{\epsilon_2} + 1/I_3^{\epsilon_2} - 2)$ [43], serving here as volumetric penalty function to account for near-incompressibility. Here, $I_1 = \text{tr}\boldsymbol{C}$ and $I_3 = \det\boldsymbol{C}$ denote the first and the third invariants of the right Cauchy-Green tensor $\boldsymbol{C} = \boldsymbol{F}^{\text{T}}\boldsymbol{F}$, while $\boldsymbol{F}$ is the deformation gradient tensor. The effect of damage is accounted for in the last part of Eq. (7) namely, the transversely isotropic part, where a so-called damage function D_i is introduced via

$$\Psi_i^{\text{ti}} = \alpha_1 \langle (1 - D_i)[\kappa I_1 + (1 - 1.5\kappa)K_3^i] - 2\rangle^{\alpha_2}, \tag{8}$$

with $i = 1, 2$ indexing fiber families (i.e., each fiber family, i, has its own damage parameter, D_i). The Macaulay brackets, $\langle(\cdot)\rangle = [(\cdot) + |(\cdot)|]/2$, filter out positive values. Here, $K_3^i = \text{tr}[\text{cof}\boldsymbol{C}(\boldsymbol{1} - \boldsymbol{M_i})]$ is the fundamental polyconvex function, introduced by Schröder and Neff [44], with the definition of the structural tensor $\boldsymbol{M_i} = \boldsymbol{A_i} \otimes \boldsymbol{A_i}$, given in terms of each fiber direction vector $\boldsymbol{A}_i$. The cofactor is defined as $\text{cof}\boldsymbol{C} = \det\boldsymbol{C}\boldsymbol{C}^{-1}$. In the case where no damage occurs, i.e. $D_i = 0$, the energy function corresponds to the one proposed in [45] which is extended by the fiber dispersion approach from [46]. The energy is polyconvex and it a *priori* ensures material stability and thus, a physically reasonable material behavior [47]. Here, c_1, ϵ_1, ϵ_2, α_1, α_2 and κ are material parameters. D_i are scalar damage functions for each fiber family $i = 1, 2$.

Acknowledgments

This work was performed with support from the IMPRS-SurMat program and by the German Research Foundation (DFG) within SFB-TRR 287/1 (project A4).

References

[1] S. Mendis, P. Puska, B. Norrving, Global atlas on cardiovascular disease prevention and control, World Health Organization in collaboration with

the World Heart Federation and the World Stroke Organization (2011) 3–18.

[2] J. Frösen, R. Tulamo, A. Paetau, E. Laaksamo, M. Korja, A. Laakso, M. Niemelä, J. Hernesniemi, Saccular intracranial aneurysm: pathology and mechanisms, Acta Neuropathol. 123 (6) (2012) 773–786.

[3] T. C. Gasser, Damage and Failure of the Vascular Wall, Springer Berlin Heidelberg, Berlin, Heidelberg, 2018, pp. 1–12.

[4] J. Tarbell, Z. Shi, J. Dunn, H. Jo, Fluid mechanics, arterial disease, and gene expression, Annu Rev Fluid Mech. 46 (2014) 591–614.

[5] J. Lee, V. Vedula, K. Baek, J. Chen, J. Hsu, Y. Ding, C. Chang, H. Kang, A. Small, P. Fei, C. Chuong, R. Li, L. Demer, R. Packard, A. Marsden, T. Hsiai, Spatial and temporal variations in hemodynamic forces initiate cardiac trabeculation, JCI insight 3 (13) (2018) e96672.

[6] J. Frösen, J. Cebral, A. Robertson, T. Aoki, Flow-induced, inflammation-mediated arterial wall remodeling in the formation and progression of intracranial aneurysms, Neurosurg Focus 47 (1) (2019) E21.

[7] L. Boussel, V. Rayz, C. McCulloch, A. Martin, G. Acevedo-Bolton, M. Lawton, R. Higashida, W. Smith, W. Young, D. Saloner, Aneurysm growth occurs at region of low wall shear stress: patient-specific correlation of hemodynamics and growth in a longitudinal study, Stroke 39 (11) (2008) 2997–3002.

[8] J. Xiang, S. Natarajan, M. Tremmel, D. Ma, J. Mocco, L. Hopkins, A. Siddiqui, E. Levy, H. Meng, Hemodynamic-morphologic discriminants for intracranial aneurysm rupture, Stroke 42 (1) (2011) 144–15.

[9] Y. Miura, F. Ishida, Y. Umeda, H. Tanemura, H. Suzuki, S. Matsushima, S. Shimosaka, W. Taki, Low wall shear stress is independently associated with the rupture status of middle cerebral artery aneurysms, Stroke 44 (2) (2013) 519–21.

[10] H. Meng, Z. Wang, Y. Hoi, L. Gao, E. Metaxa, D. Swartz, J. Kolega, Complex hemodynamics at the apex of an arterial bifurcation induces vascular remodeling resembling cerebral aneurysm initiation, Stroke 38 (2007) 1924–31.

[11] M. Castro, C. Putman, M. Sheridan, J. Cebral, Hemodynamic patterns of anterior communicating artery aneurysms: a possible association with rupture, AJNR Am J Neuroradiol 30 (2009) 297–302.

[12] J. R. Cebral, F. Mut, J. Weir, C. M. Putman, Quantitative characterization of the hemodynamic environment in ruptured and unruptured brain aneurysms, AJNR Am J Neuroradiol 32 (1) (2011) 145–151.

[13] H. Meng, V. M. Tutino, J. Xiang, A. Siddiqui, High WSS or Low WSS? Complex interactions of hemodynamics with intracranial aneurysm initiation, growth, and rupture: Toward a unifying hypothesis, American Journal of Neuroradiology 35 (7) (2014) 1254–1262.

[14] H. Wang, T. Krüger, F. Varnik, Effects of size and elasticity on the relation between flow velocity and wall shear stress in side-wall aneurysms: A lattice Boltzmann-based computer simulation study, PLoS ONE 15 (1) (2020) e0227770.

[15] D. Balzani, S. Deparis, S. Fausten, D. Forti, A. Heinlein, A. Klawonn, A. Quarteroni, O. Rheinbach, J. Schröder, Numerical modeling of fluid–structure interaction in arteries with anisotropic polyconvex hyperelastic and anisotropic viscoelastic material models at finite strains, Int J Numer Method Biomed Eng 32 (10).

[16] D. Balzani, S. Brinkhues, G. Holzapfel, Constitutive framework for the modeling of damage in collagenous soft tissues with application to arterial walls, Comput. Methods Appl. Mech. Engrg. 213-216 (2012) 139–151.

[17] E. Anttila, D. Balzani, A. Desyatova, P. Deegan, J. MacTaggart, A. Kamenskiy, Mechanical damage characterization in human femoropopliteal arteries of different ages, Acta Biomaterialia. 90 (6) (2019) 225–240.

[18] SimVascular/svFSI. [link].
URL `https://github.com/SimVascular/svFSI`

[19] B. Calvo, E. Peña, M. Martínez, M. Doblaré, An uncoupled directional damage model for fibered biological soft tissues, Int J Numer Methods 69 (2007) 2036–2057.

[20] A. Ehret, M. Itskov, Modeling of anisotropic softening phenomena: Application to soft biological tissues, Int J Plast 25 (2009) 901–919.

[21] H. Weisbecker, D. Pierce, P. Regitnig, G. Holzapfel, Layer-specific damage experiments and modeling of human thoracic and abdominal aortas with non-atherosclerotic intimal thickening, J Mech Behav Biomed Mater 12 (2012) 93–106.

[22] N. Famaey, J. Vander Sloten, E. Kuhl, A three-constituent damage model for arterial clamping in computer-assisted surgery, Biomech Model Mechanobiol 12 (2013) 123–136.

[23] D. Balzani, M. Ortiz, Relaxed incremental variational formulation for damage at large strains with application to fiber-reinforced materials and materials with truss-like microstructures, Int J Numer Methods Eng 92 (2012) 551–570.

[24] T. Waffenschmidt, C. Polindara, A. Menzel, S. Blanco, A gradient-enhanced large-deformation continuum damage model for fibre-reinforced materials, Comput Methods Appl Mech Eng 268 (2014) 801–842.

[25] V. Vedula, J. Lee, H. Xu, C. Kuo, T. Hsiai, A. Marsden, A method to quantify mechanobiologic forces during zebrafish cardiac development using 4-D light sheet imaging and computational modeling, PLoS Comput Biol. 13 (10) (2017) e1005828.

[26] J. Seo, D. Schiavazzi, A. Marsden, Performance of preconditioned iterative linear solvers for cardiovascular simulations in rigid and deformable vessels, Comput Mech 64 (3) (2019) 717–739.

[27] K. Bäumler, V. Vedula, A. Sailer, J. Seo, P. Chiu, G. Mistelbauer, F. Chan, M. Fischbein, A. Marsden, Fluid-structure interaction simulations of patient-specific aortic dissection, Biomech Model Mechanobiol. 19 (2020) 1607–1628.

[28] M. Lehecka, R. Dashti, R. Romani, O. Çelik, O. Navratil, L. Kivipelto, R. Kivisaari, H. Shen, K. Ishii, Microneurosurgical management of internal carotid artery bifurcation aneurysms, Surgical Neurology 71 (6) (2009) 649–667.

[29] C. Chnafa, P. Bouillot, O. Brina, B. Delattre, M. Vargas, K. Lovblad, V. Pereira, D. Steinman, Vessel calibre and flow splitting relationships at the internal carotid artery terminal bifurcation, Physiol Meas. 38 (11) (2017) 2044–2057.

[30] A. Usmani, K. Muralidhar, Flow in an intracranial aneurysm model: effect of parent artery orientation, J Vis 21 (2018) 795–818.

[31] S. Lee, L. Antiga, J. Spence, D. Steinman, Geometry of the carotid bifurcation predicts its exposure to disturbed flow, Stroke 39 (8) (2008) 2341–7.

[32] M. Kroon, G. A. Holzapfel, Estimation of the distributions of anisotropic, elastic properties and wall stresses of saccular cerebral aneurysms by inverse analysis, Proc. R. Soc. A 464 (2008) 807–825.

[33] T. Khamdaeng, J. Luo, J. Vappou, P. Terdtoon, E. Konofagou, Arterial stiffness identification of the human carotid artery using the stress-strain relationship in vivo, Ultrasonics 52 (3) (2012) 402–411.

[34] J. Blacher, A. Evans, D. Arveiler, P. Amouyel, J. Ferrières, A. Bingham, J. Yarnell, B. Haas, M. Montaye, J. Ruidavets, P. Ducimetière, Prime study group. residual cardiovascular risk in treated hypertension and hyperlipidaemia: the prime study, J Hum Hypertens. 24 (1) (2010) 19–26.

[35] B. Aribisala, Z. Morris, E. Eadie, A. Thomas, A. Gow, H. M. Valdés, N. Royle, M. Bastin, J. Starr, I. Deary, J. Wardlaw, Blood pressure, internal carotid artery flow parameters, and age-related white matter hyperintensities, Hypertension 63 (5) (2014) 1011–8.

[36] H. Kim, I. Vignon-Clementel, C. Figueroa, K. Jansen, C. Taylor, Developing computational methods for three-dimensional finite element simulations of coronary blood flow, Finite Elem Anal Des 46 (6) (2010) 514–525.

[37] D. M. Sforza, C. M. Putman, J. R. Cebral, Hemodynamics of Cerebral Aneurysms, Annu Rev Fluid Mech 41 (2009) 91–107.

[38] T. Yagi, A. Sato, M. Shinke, S. Takahashi, Y. Tobe, H. Takao, Y. Murayama, M. Umezu, Experimental insights into flow impingement in cerebral aneurysm by stereoscopic particle image velocimetry: Transition from a laminar regime, J R Soc. Interface 10 (82) (2013) 20121031.

[39] D. Balzani, D. Böse, D. Brands, R. Erbel, A. Klawonn, O. Rheinbach, J. Schröder, Parallel simulation of patient-specific atherosclerotic arteries for the enhancement of intravascular ultrasound diagnostics, Engrg Comput 29 (8) (2012) 888–906.

[40] F. Kong, V. Kheyfets, E. Finol, X. Cai, An efficient parallel simulation of unsteady blood flows in patient-specific pulmonary artery, Int J Numer Method Biomed Eng 34 (2018) e2952.

[41] J. Allcock, P. Canham, Angiographic study of the growth of intracranial aneurysms, J Neurosurg. 45 (6) (1976) 617–621.

[42] J. R. Cebral, F. Detmer, B. Chung, J. Choque-Velasquez, B. Rezai, H. Lehto, R. Tulamo, J. Hernesniemi, M. Niemela, A. Yu, R. Williamson, K. Aziz, S. Sakur, S. Amin-Hanjani, F. Charbel, Y. Tobe, A. Robertson, J. Frösen, Local hemodynamic conditions associated with focal changes in the intracranial aneurysm wall, AJNR Am J Neuroradiol 40 (3) (2019) 510–516.

[43] S. Hartmann, P. Neff, Existence theory for a modified polyconvex hyperelastic relation of generalized polynomial-type in the case of nearly-incompressibility, Int J. Solids Struct 40 (2003) 2767–2791.

[44] J. Schröder, P. Neff, Invariant formulation of hyperelastic transverse isotropy based on polyconvex free energy functions, International Journal of Solids and Structures 40 (2) (2003) 401–445.

[45] D. Balzani, P. Neff, J. Schröder, G. Holzapfel, A polyconvex framework for soft biological tissues. Adjustment to experimental data, Int J. Solids Struct 43 (20) (2006) 6052–6070.

[46] T. C. Gasser, R. Ogden, G. Holzapfel, Hyperelastic modelling of arterial layers with distributed collagen fibre orientations, J R Soc. Interface 3 (2006) 15–35.

[47] J. Schröder, P. Neff, D. Balzani, A variational approach for materially stable anisotropic hyperelasticity, Int J. Solids Struct 42 (15) (2005) 4352–4371.